

## Applications of plane-wave destruction filters

Sergey Fomel\*

### ABSTRACT

Plane-wave destruction filters originate from a local plane-wave model for characterizing seismic data. These filters can be thought of as a time-distance ( $T$ - $X$ ) analog of frequency-distance ( $F$ - $X$ ) prediction-error filters and as an alternative to  $T$ - $X$  prediction-error filters. The filters are constructed with the help of an implicit finite-difference scheme for the local plane-wave equation. Several synthetic and real data examples show that finite-difference plane-wave destruction filters perform well in applications such as fault detection, data interpolation, and noise attenuation.

### INTRODUCTION

Plane-wave destruction filters, introduced by Claerbout (1992), characterize seismic images by a superposition of local plane waves. They are constructed as finite-difference stencils for the plane-wave differential equation. In many cases, a local plane-wave model is a very convenient representation of seismic data. Unfortunately, early experiences with applying plane-wave destructors for interpolating spatially aliased data (Nichols, 1990; Claerbout, 1992) demonstrated their poor performance in comparison with industry-standard frequency-distance ( $F$ - $X$ ) prediction-error filters (Spitz, 1991).

For each given frequency, an  $F$ - $X$  prediction error filter (PEF) can be thought of as a  $z$ -transform polynomial. The roots of the polynomial correspond precisely to predicted plane waves (Canales, 1984). Therefore,  $F$ - $X$  PEFs simply represent a spectral (frequency-domain) approach to plane-wave destruction. (The filters are designed to destroy local plane waves. However, in applications such as data interpolation, they are often used to reconstruct the missing parts of local waves. The choice of terminology should not confuse the reader.) This powerful and efficient approach is, however, theoretically inadequate when the plane-wave slopes or the boundary conditions vary both spatially and temporally. In practice, this limitation is addressed by breaking the data into windows and assuming that the slopes are stationary within each window.

Multidimensional time-distance ( $T$ - $X$ ) prediction-error filters (Claerbout, 1992, 1999) share the same purpose: to predict local plane waves. They work well with spatially aliased data and allow for both temporal and spatial variability of the slopes. In practice, however,  $T$ - $X$  filters appear as very mysterious objects because their construction involves many nonintuitive parameters. The user needs to choose several parameters, such as the number of filter coefficients; the gap and the exact shape of the filter; the size, number, and shape of local patches for filter estimation; the number of iterations; and the amount of regularization. Recently developed techniques for handling nonstationary PEFs (Crawley et al., 1999) performed well in a variety of applications (Crawley, 2000; Guitton et al., 2001), but the large number of adjustable parameters still requires a significant level of human interaction and remains the main drawback of the method.

Clapp et al. (1998) have revived the original plane-wave destructors for preconditioning tomographic problems with a pre-defined dip field (Clapp, 2000). The filters are named steering filters because of their ability to steer the solution in the direction of the local dips. The name is also reminiscent of steerable filters, used in medical image processing (Freeman and Adelson, 1991; Simoncelli and Farid, 1996).

In this paper, I revisit Claerbout's original technique of finite-difference plane-wave destruction. First, I introduce an approach for increasing the accuracy and dip bandwidth of the method. Applying the improved filter design to several data regularization problems, I show that the finite-difference filters often perform as well as, or even better than,  $T$ - $X$  PEFs. At the same time, they keep the number of adjustable parameters to a minimum, and the only estimated quantity has a clear physical meaning of the local plane-wave slope. No local windows are required because the slope is estimated as a smoothly variable continuous function of the data coordinates.

Conventional methods for estimating plane-wave slopes are based on picking maximum values of stacking semblance and other cumulative coherency measures (Neidell and Taner, 1971). The differential approach to slope estimation, used by plane-wave destruction filters, is related to the differential

Manuscript received by the Editor November 22, 2000; revised manuscript received April 15, 2002.

\*Formerly Lawrence Berkeley National Laboratory, Mail Stop 50A-1148, 1 Cyclotron Road, Berkeley, California 94720; presently Bureau of Economic Geology, University of Texas at Austin, University Station, Box X, Austin, Texas 78713-8924. E-mail: sergey.fomel@utexas.edu.

© 2002 Society of Exploration Geophysicists. All rights reserved.

semblance method (Symes and Carazzone, 1991). Its theoretical superiority to conventional semblance measures for the problem of local plane-wave detection has been established by Symes (1994) and Kim and Symes (1998).

### HIGH-ORDER PLANE-WAVE DESTRUCTORS

Following the physical model of local plane waves, we can define the mathematical basis of the plane-wave destruction filters as the local plane differential equation

$$\frac{\partial P}{\partial x} + \sigma \frac{\partial P}{\partial t} = 0, \quad (1)$$

where  $P(t, x)$  is the wavefield and  $\sigma$  is the local slope, which may also depend on  $t$  and  $x$ . In the case of a constant slope, equation (1) has the simple general solution

$$P(t, x) = f(t - \sigma x), \quad (2)$$

where  $f(t)$  is an arbitrary waveform. Equation (2) is nothing more than a mathematical description of a plane wave.

If we assume that  $\sigma$  does not depend on  $t$ , we can transform equation (1) to the frequency domain, where it takes the form of the ordinary differential equation

$$\frac{d\hat{P}}{dx} + i\omega\sigma\hat{P} = 0 \quad (3)$$

and has the general solution

$$\hat{P}(x) = \hat{P}(0) e^{i\omega\sigma x}, \quad (4)$$

where  $\hat{P}$  is the Fourier transform of  $P$ . The complex exponential term in equation (4) represents a shift of a  $t$ -trace according to the slope  $\sigma$  and the trace separation  $x$ .

In the frequency domain, the operator for transforming the trace at position  $x - 1$  to the neighboring trace at position  $x$  is a multiplication by  $e^{i\omega\sigma}$ . (For simplicity, assume  $x$  takes integer values that correspond to trace numbering.) In other words, a plane wave can be predicted perfectly by a two-term prediction-error filter in the  $F$ - $X$  domain:

$$a_0 \hat{P}(x) + a_1 \hat{P}(x - 1) = 0, \quad (5)$$

where  $a_0 = 1$  and  $a_1 = -e^{i\omega\sigma}$ . The goal of predicting several plane waves can be accomplished by cascading several two-term filters. In fact, any  $F$ - $X$  prediction-error filter represented in the  $z$ -transform notation as

$$A(Z_x) = 1 + a_1 Z_x + a_2 Z_x^2 + \dots + a_N Z_x^N \quad (6)$$

can be factored into a product of two-term filters:

$$A(Z_x) = \left(1 - \frac{Z_x}{Z_1}\right) \left(1 - \frac{Z_x}{Z_2}\right) \dots \left(1 - \frac{Z_x}{Z_N}\right), \quad (7)$$

where  $Z_1, Z_2, \dots, Z_N$  are the zeroes of polynomial (6). According to equation (5), the phase of each zero corresponds to the slope of a local plane wave multiplied by the frequency. Zeroes that are not on the unit circle carry an additional amplitude gain not included in equation (3).

To incorporate time-varying slopes, we need to return to the time domain and look for an appropriate analog of the phase-shift operator [equation (4)] and the plane-prediction filter [equation (5)]. An important property of plane-wave propagation across different traces is that the total energy of

the propagating wave stays invariant, throughout the process: the energy of the wave at one trace is completely transmitted to the next trace. This property is assured in the frequency-domain solution [equation (4)] by the fact that the spectrum of the complex exponential  $e^{i\omega\sigma}$  equals one. In the time domain, we can reach an equivalent effect by using an all-pass digital filter. In the  $z$ -transform notation, convolution with an all-pass filter takes the form

$$\hat{P}_{x+1}(Z_t) = \hat{P}_x(Z_t) \frac{B(Z_t)}{B(1/Z_t)}, \quad (8)$$

where  $\hat{P}_x(Z_t)$  denotes the  $Z$ -transform of the corresponding trace, and the ratio  $B(Z_t)/B(1/Z_t)$  is an all-pass digital filter approximating the time-shift operator  $e^{i\omega\sigma}$ . In finite-difference terms, equation (8) represents an implicit finite-difference scheme for solving equation (1) with the initial conditions at a constant  $x$ . The coefficients of filter  $B(Z_t)$  can be determined, for example, by fitting the filter frequency response at low frequencies to the response of the phase-shift operator. The Taylor series technique (equating the coefficients of the Taylor series expansion around zero frequency) yields the expression

$$B_3(Z_t) = \frac{(1 - \sigma)(2 - \sigma)}{12} Z_t^{-1} + \frac{(2 + \sigma)(2 - \sigma)}{6} + \frac{(1 + \sigma)(2 + \sigma)}{12} Z_t \quad (9)$$

for a three-point centered filter  $B_3(Z_t)$  and the expression

$$B_5(Z_t) = \frac{(1 - \sigma)(2 - \sigma)(3 - \sigma)(4 - \sigma)}{1680} Z_t^{-2} + \frac{(4 - \sigma)(2 - \sigma)(3 - \sigma)(4 + \sigma)}{420} Z_t^{-1} + \frac{(4 - \sigma)(3 - \sigma)(3 + \sigma)(4 + \sigma)}{280} + \frac{(4 - \sigma)(2 + \sigma)(3 + \sigma)(4 + \sigma)}{420} Z_t + \frac{(1 + \sigma)(2 + \sigma)(3 + \sigma)(4 + \sigma)}{1680} Z_t^2 \quad (10)$$

for a five-point centered filter  $B_5(Z_t)$ . The derivation of equations (9) and (10) is detailed in the appendix. It is easy to generalize these equations to longer filters. Figure 1 shows the phase of the all-pass filters  $B_3(Z_t)/B_3(1/Z_t)$  and  $B_5(Z_t)/B_5(1/Z_t)$  for two values of the slope  $\sigma$  in comparison with the exact linear function of equation (4). As expected, the phases match the exact line at low frequencies, and the accuracy of the approximation increases with the length of the filter.

Taking both dimensions into consideration, equation (8) transforms to the prediction equation analogous to equation (5) with the 2-D prediction filter:

$$A(Z_t, Z_x) = 1 - Z_x \frac{B(Z_t)}{B(1/Z_t)}. \quad (11)$$

To characterize several plane waves, we can cascade several filters of the form (11) in a manner similar to that of equation (7). In this paper, I use a modified version of the filter  $A(Z_t, Z_x)$ , namely the filter

$$C(Z_t, Z_x) = A(Z_t, Z_x)B\left(\frac{1}{Z_t}\right) = B\left(\frac{1}{Z_t}\right) - Z_x B(Z_t), \quad (12)$$

which avoids the need for polynomial division. In case of the three-point filter [equation (9)], the 2-D filter [equation (12)] has exactly six coefficients. It consists of two columns, each column having three coefficients and the second column being a reversed copy of the first one. When filter (12) is used in data regularization problems, it can occasionally cause undesired high-frequency oscillations in the solution, resulting from the near-Nyquist zeroes of the polynomial  $B(Z_t)$ . The oscillations are easily removed in practice with appropriate low-pass filtering.

### SLOPE ESTIMATION

In this section, I address the problem of estimating the local slope  $\sigma$  with filters of form (12). Estimating the slope is a necessary step for applying the finite-difference plane-wave filters on real data.

Let us denote by  $\mathbf{C}(\sigma)$  the operator of convolving the data with the 2-D filter  $C(Z_t, Z_x)$  of equation (12), assuming the local slope  $\sigma$  is known. To determine the slope, we can define the least-squares goal

$$\mathbf{C}(\sigma) \mathbf{d} \approx 0, \quad (13)$$

where  $\mathbf{d}$  is the known data and the approximate equality implies that the solution is found by minimizing the power of the left-hand side. Equations (9) and (10) show that the slope  $\sigma$  enters in the filter coefficients in an essentially nonlinear way. However, one can still apply the linear iterative optimization methods by an analytical linearization of equation (13). The linearization (also known as the Gauss-Newton iteration) implies solving the linear system

$$\mathbf{C}'(\sigma_0) \Delta\sigma \mathbf{d} + \mathbf{C}(\sigma_0) \mathbf{d} \approx 0 \quad (14)$$

for the slope increment  $\Delta\sigma$ . Here  $\sigma_0$  is the initial slope estimate and  $\mathbf{C}'(\sigma)$  is a convolution with the filter, obtained by differentiating the filter coefficients of  $\mathbf{C}(\sigma)$  with respect to  $\sigma$ . After system (14) is solved, the initial slope  $\sigma_0$  is updated by adding  $\Delta\sigma$  to it, and one can solve the linear problem again. Depending on the starting solution, the method may require several nonlinear iterations to achieve an acceptable convergence.

The slope  $\sigma$  in equation (14) does not have to be constant. We can consider it as varying in both time and space coordinates. This eliminates the need for local windows but may lead to undesirably rough (oscillatory) local slope estimates. Moreover, the solution will be undefined in regions of unknown

or constant data because for these regions the local slope is not constrained. Both of these problems are solved by adding a regularization (styling) goal to system (14). The additional goal takes the form

$$\epsilon \mathbf{D} \Delta\sigma \approx 0, \quad (15)$$

where  $\mathbf{D}$  is an appropriate roughening operator and  $\epsilon$  is a scaling coefficient. For simplicity, I chose  $\mathbf{D}$  as the gradient operator. More efficient and sophisticated helical preconditioning techniques are available (Claerbout, 1998; Fomel, 2000; Fomel and Claerbout, 2003).

In theory, estimating two different slopes  $\sigma_1$  and  $\sigma_2$  from the available data is only marginally more complicated than estimating a single slope. The convolution operator becomes a cascade of  $\mathbf{C}(\sigma_1)$  and  $\mathbf{C}(\sigma_2)$ , and the linearization yields

$$\begin{aligned} \mathbf{C}'(\sigma_1) \mathbf{C}(\sigma_2) \Delta\sigma_1 \mathbf{d} + \mathbf{C}(\sigma_1) \mathbf{C}'(\sigma_2) \Delta\sigma_2 \mathbf{d} \\ + \mathbf{C}(\sigma_1) \mathbf{C}(\sigma_2) \mathbf{d} \approx 0. \end{aligned} \quad (16)$$

The regularization condition should now be applied to both  $\Delta\sigma_1$  and  $\Delta\sigma_2$ :

$$\epsilon \mathbf{D} \Delta\sigma_1 \approx 0, \quad (17)$$

$$\epsilon \mathbf{D} \Delta\sigma_2 \approx 0. \quad (18)$$

The solution obviously depends on the initial values of  $\sigma_1$  and  $\sigma_2$ , which should not equal each other. System (16) is generally underdetermined because it contains twice as many estimated parameters as equations: The number of equations corresponds to the grid size of the data  $\mathbf{d}$ , while characterizing variable slopes  $\sigma_1$  and  $\sigma_2$  on the same grid involves two gridded functions. However, an appropriate choice of the starting solution and the additional regularization [equations (17) and (18)] allow us to arrive at a practical solution.

The application examples of the next section demonstrate that when the system of equations (14)–(15) or (16)–(18) is optimized in the least-squares sense in a cycle of several linearization iterations, the result is smooth and reliable slope estimates. The regularization conditions (15), (17), and (18) ensure a smooth extrapolation of the slope to the regions of unknown or constant data.

### APPLICATION EXAMPLES

Let us examine the performance of the finite-difference plane-destruction filters on several test applications. The

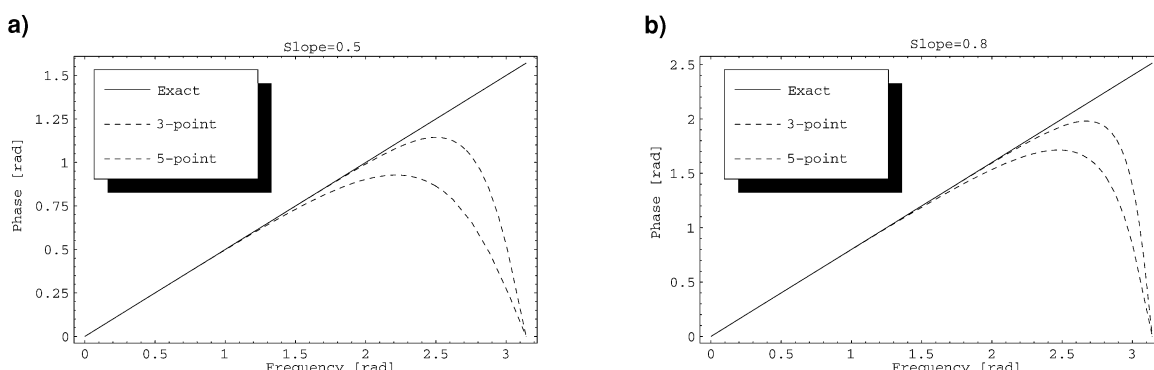


FIG. 1. Phase of the implicit finite-difference shift operators in comparison with the exact solution. (a) Slope  $\sigma = 0.5$ . (b) Slope  $\sigma = 0.8$ .

general framework for applying these filters consists of two steps.

First we estimate the dominant local slope (or a set of local slopes) from the data. This step follows the least-squares optimization embedded in equation (14) or (16). Thanks to the general regularization technique of equations (15), (17), and (18), locally smooth slope estimates are obtained without need to break the data into local windows. Of course, local windows can be used for other purposes (parallelization, memory management, etc.). Selecting appropriate initial values for the local slopes can speed up the computation and steer it toward desirable results. It is easy to incorporate additional constraints on the local slope values.

Second, using the estimated slope, apply nonstationary plane-wave destruction filters for the particular application purposes. In the fault detection application, we look at the output of plane-wave destruction. In the interpolation application, the filters are used to constrain the missing data. In the noise attenuation application, they characterize the coherent signal and noise components in the data.

### Fault detection

The use of prediction-error filters in the problem of detecting local discontinuities was suggested by Claerbout (1994, 1999) and further refined by Schwab et al. (1996) and Schwab (1998). Bednar (1998) uses simple plane-destruction filters in a similar setting to compute coherency attributes.

To test the performance of the improved plane-wave destructors, I chose several examples from Claerbout (1999). Figure 2a shows a synthetic model that resembles sedimentary layers with a plane unconformity and a curvilinear fault. The model contains 200 traces of 200 samples each. Figure 2b shows the corresponding texture (Claerbout and Brown, 1999), obtained by convolving a field of random numbers with the inverse of

plane-wave destruction filters. The inverses are constructed using helical filtering techniques (Claerbout, 1998; Fomel, 2000). Texture plots allow us to quickly access the ability of the destruction filters to characterize the main locally plane features in the data. The dip field was estimated by the linearization method of the previous section.

The dip field itself and the prediction residual [the left-hand side of equation (13)] are shown in Figure 3. The texture plot does reflect the dip structure of the input data, which indicates that the dip field was estimated correctly. The fault and unconformity are clearly visible both in the dip estimate and in the residual plots. Anywhere outside the slope discontinuities and the boundaries, the residual is close to zero. Therefore, it can be used directly as a fault detection measure. Comparing the residual plot in Figure 3 with the analogous plot of Claerbout (1994, 1999), reproduced in Figure 4, establishes a superior performance of the improved finite-difference destructors in comparison with that of the local  $T$ - $X$  prediction-error filters.

Figure 5a introduces a simpler synthetic test. The model is composed of linear events with two conflicting slopes. A regularized dip field estimation attempts to smooth the estimated dip in the places where it is not constrained by the data (Figure 6a). The effect of smoothing is clearly seen in the texture image (Figure 5b). The corresponding residual (Figure 6b) shows suppressed linear events and highlights where they intersect. Residuals are large at intersections because a single dominant dip model fails to adequately represent both conflicting dips.

Figure 7a shows a real shot gather—a portion of Yilmaz and Cumro's (1983) data set 27. The initial dip in the dip estimation program was set to zero. Therefore, the texture image (Figure 7b) contains zero-dipping plane waves in places of no data. Everywhere else the dip is accurately estimated from the data. The data contain a missing trace at about 0.7 km offset and a slightly shifted (possibly mispositioned) trace at about

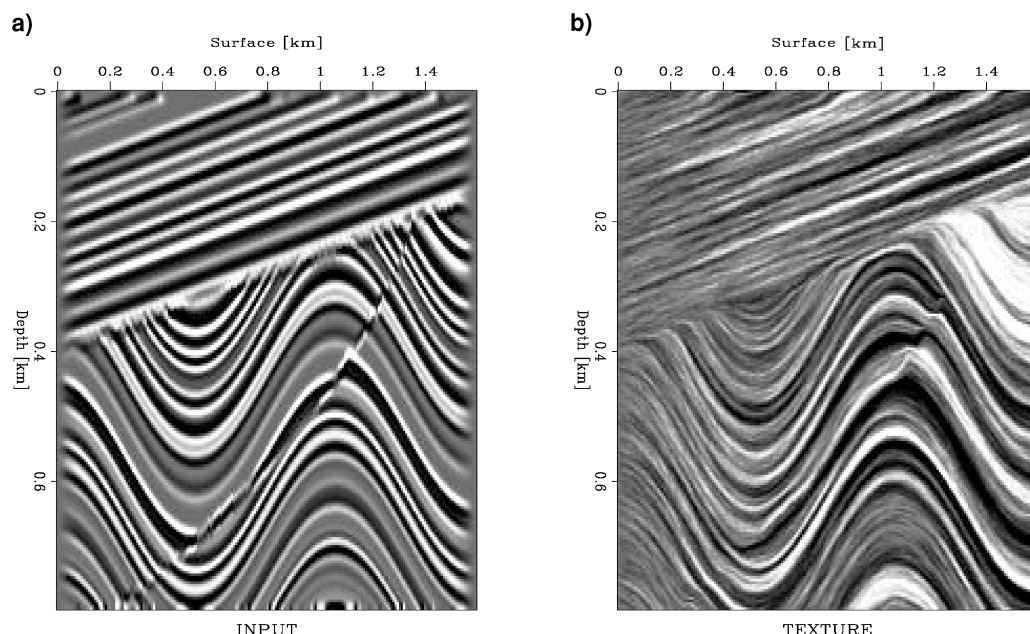


FIG. 2. Synthetic sedimentary model. (a) Input data. (b) Its texture. The texture is computed by convolving a field number with the inverse of plane-wave destruction filters. It highlights the position of estimated local plane waves.

1.1 km offset. The mispositioned trace is clearly visible in the dip estimate (Figure 8a), and the missing trace is emphasized in the residual image (Figure 8b). Additionally, the residual image reveals the forward and back-scattered surface waves, hidden under more energetic reflections in the input data.

Figure 9 shows a stacked time section from the Gulf of Mexico and its corresponding texture. The texture plot demonstrates that the estimated dip (Figure 10a) reflects the dominant local dip in the data. After the plane waves with the dominant dip are removed, many hidden diffractions appear in the residual image (Figure 10b). The enhanced diffraction events can be used, for example, to estimate the medium velocity (Harlan et al., 1984).

Overall, the examples of this subsection show that the finite-difference plane-wave destructors provide a reliable tool for enhancing of discontinuities and conflicting slopes in seismic images. The estimation step of the fault detection procedure produces an image of the local dominant dip field, which may have its own interpretational value. An extension to 3-D is possible, as outlined by Schwab (1998), Clapp (2000), and Fomel (2000).

#### Trace interpolation beyond aliasing

Spitz (1991) popularized the application of prediction-error filters to regular trace interpolation and showed how the spatial aliasing restriction can be overcome by scaling the lower frequencies of  $F$ - $X$  PEFs. An analogous technique for  $T$ - $X$  filters was developed by Claerbout (1992, 1999) and was applied for 3-D interpolation with nonstationary PEFs by Crawley (2000). The  $T$ - $X$  technique implies stretching the filter in all directions so that its dip spectrum is preserved while the coefficients are estimated at alternating traces. After the filter is estimated, it is scaled back and used for interpolating miss-

ing traces between the known ones. A very similar method works for finite-difference plane-wave destructors, only we need to take special care of the aliased dips at the dip estimation stage.

A simple synthetic example of interpolation beyond aliasing is shown in Figure 11. The input data are clearly aliased and nonstationary. To take the aliasing into account, I estimate the two dips present in the data with the slope estimation technique of equations (16)–(18). The first dip corresponds to the true slope, while the second dip corresponds to the aliased

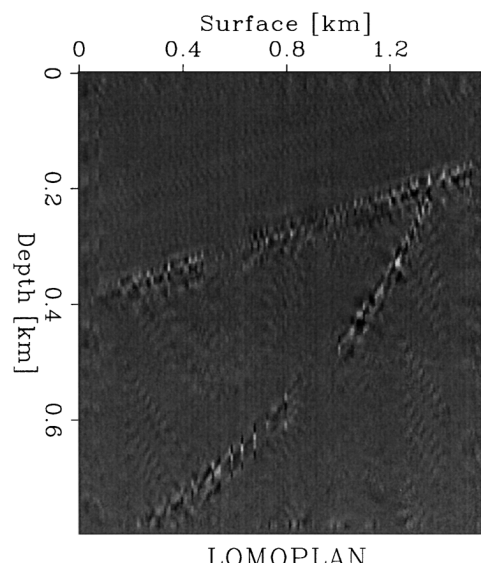


FIG. 4. Prediction residual of the 11-point prediction-error filter (lomoplan) estimated in local  $20 \times 6$  windows [reproduced from Claerbout (1999)]. Compare with Figure 3b.

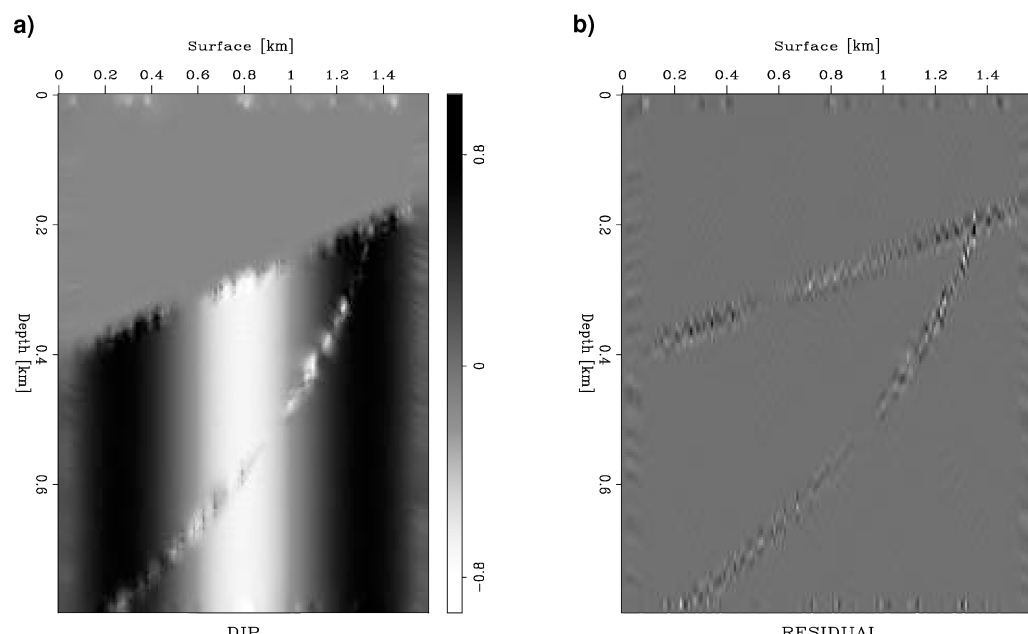


FIG. 3. Synthetic sedimentary model. (a) Estimated dip field. (b) Prediction residual. A large absolute residual indicates the location of faults.

dip component. In this example, the true dip is nonnegative everywhere and is easily distinguished from the aliased one. In the more general case, an additional interpretation may be required to determine which of the dip components is contaminated by aliasing. Throwing away the aliased dip and interpolating intermediate traces with the true dip produces the accurate interpolation result shown in Figure 11b. Three additional traces were inserted between each of the neighboring input traces.

Figure 12 shows a marine 2-D shot gather from a deepwater Gulf of Mexico survey before and after subsampling in the

offset direction. The data are similar to those used by Crawley (2000). The shot gather has long-period multiples and complicated diffraction events caused by a salt body. The amplitudes of the hyperbolic events are not as uniformly distributed as in the synthetic case of Figure 11. Subsampling by a factor of two (Figure 12b) causes clearly visible aliasing in the steeply dipping events. The goal of the experiment is to interpolate the missing traces in the subsampled data and to compare the result with the original gather (Figure 12a).

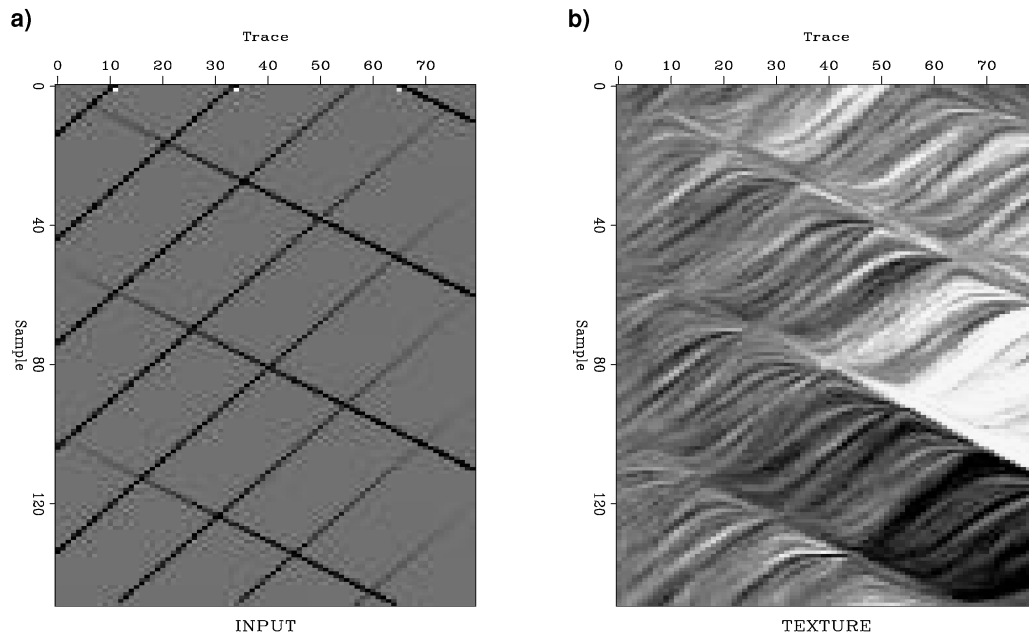


FIG. 5. Conflicting dips synthetic. (a) Input data. (b) Its texture.

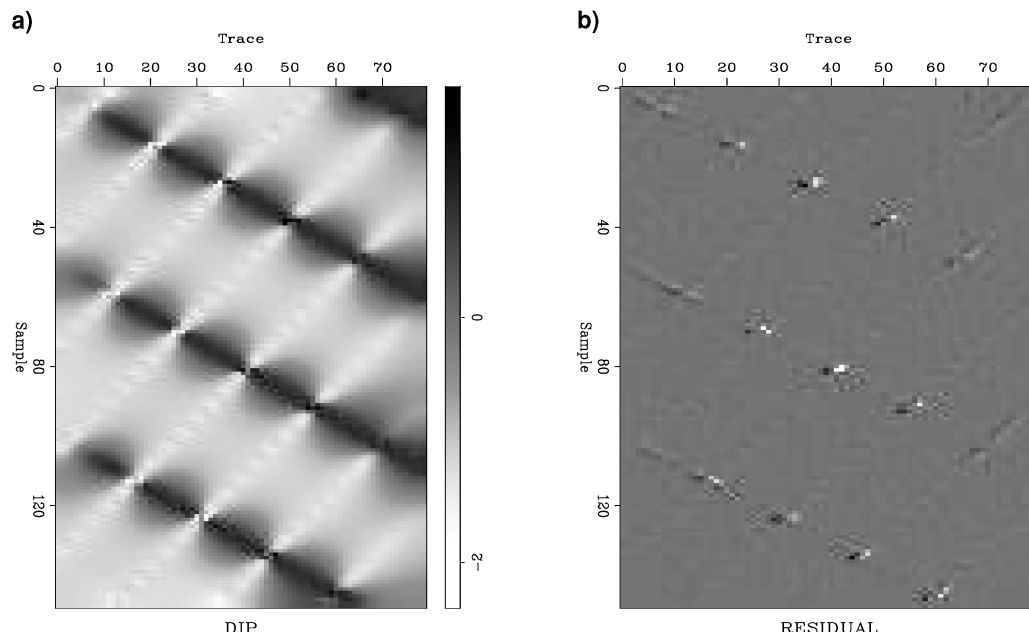


FIG. 6. Conflicting dips synthetic. (a) Estimated dip field. (b) Prediction residual. Large absolute residual indicates the location of conflicting dips.

A straightforward application of the dip estimation equations (16)–(18) applied to aliased data can easily lead to erroneous aliased dip estimation because the aliased dip may get picked instead of the true dip. To avoid this problem, I chose a slightly more complex strategy. The algorithm for trace interpolation of aliased data consists of the following steps.

- 1) Applying Claerbout's  $T$ - $X$  methodology, stretch a two-dip plane-wave destruction filter and estimate the dips from decimated data.
- 2) Ignore this initial second-dip estimate because it might be degraded by aliasing.

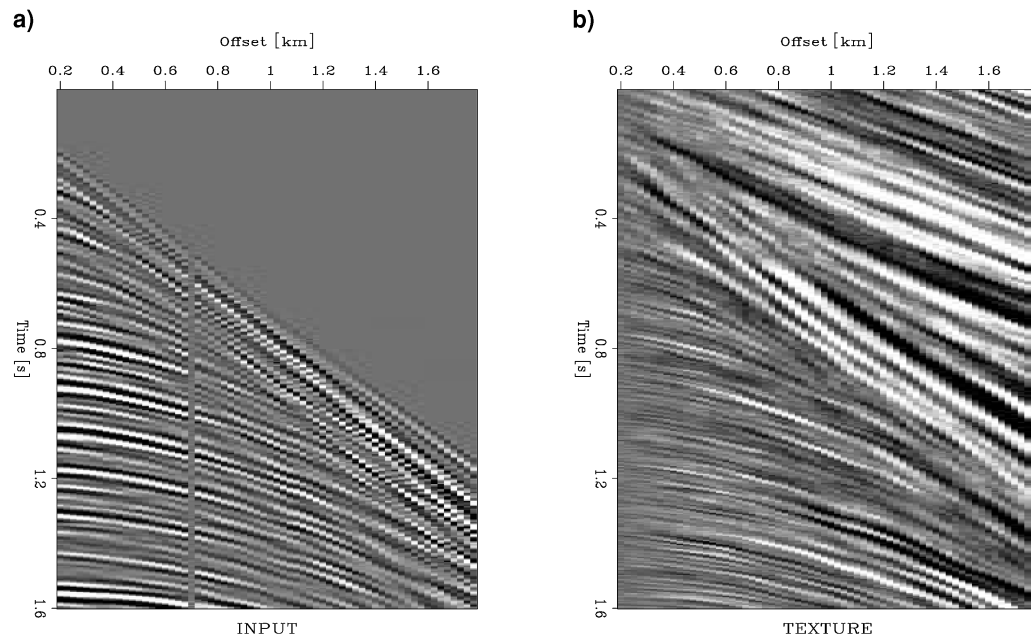


FIG. 7. Real shot gather. (a) Input data. (b) Its texture.

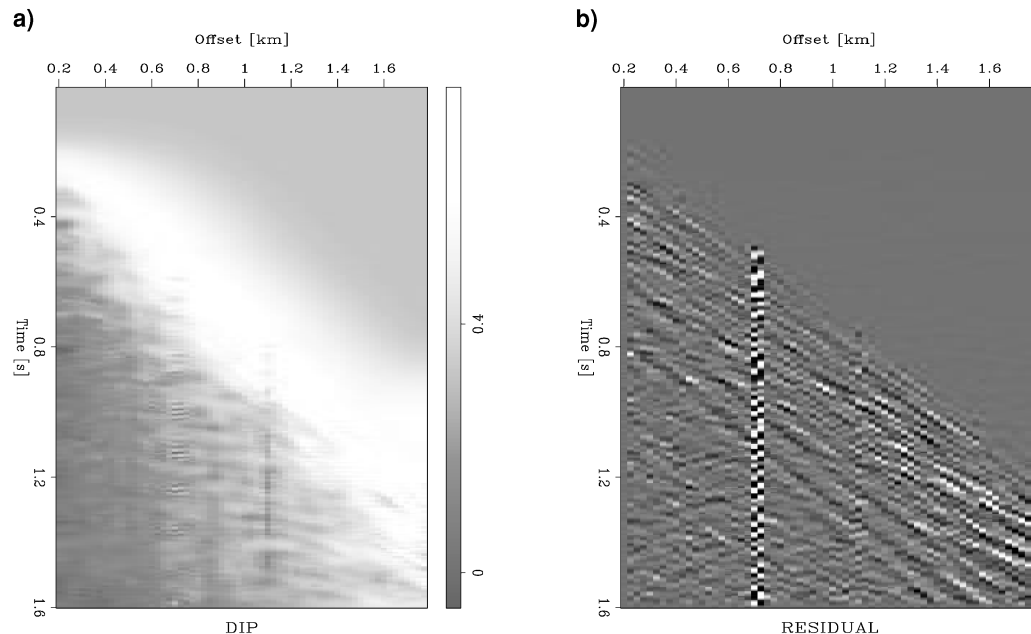


FIG. 8. Real shot gather. (a) Estimated dip field. (b) Prediction residual. The residual highlights surface waves hidden under dominant reflection events in the original data.

- 3) Estimate the second dip component again by fixing the first dip component and using it as the initial estimate of the second component. This trick prevents the nonlinear estimation algorithm from picking the wrong (aliased) dip in the data.
- 4) Downscale the estimated two-dip filter and use it for interpolating missing traces.

The two estimated dip components are shown in Figure 13. The first component (Figure 13a) contains only positive dips. The second component (Figure 13b) coincides with the first in the areas where only a single dip is present in the data. In

other areas, it picks the complementary dip, which has a negative value for back-dipping hyperbolic diffractions.

Figure 14 shows the interpolation result and the difference between the interpolated traces and the original traces, plotted at the same clip value. The method succeeded in the sense that it is impossible to distinguish interpolated traces from the interpolation result alone. However, it is not ideal because some of the original energy is missing in the output. A close-up comparison between the original and the interpolated traces

(Figure 15) shows the imperfection in more detail. Some of the steepest events in the middle of the section are poorly interpolated; in some of the other places, the second-dip component is continued instead of the first one.

One could improve the interpolation result considerably by including another dimension. To achieve a better result, we can use a pair of plane-wave destructors—one predicting local plane waves in the offset direction and the other predicting local plane waves in the shot direction.

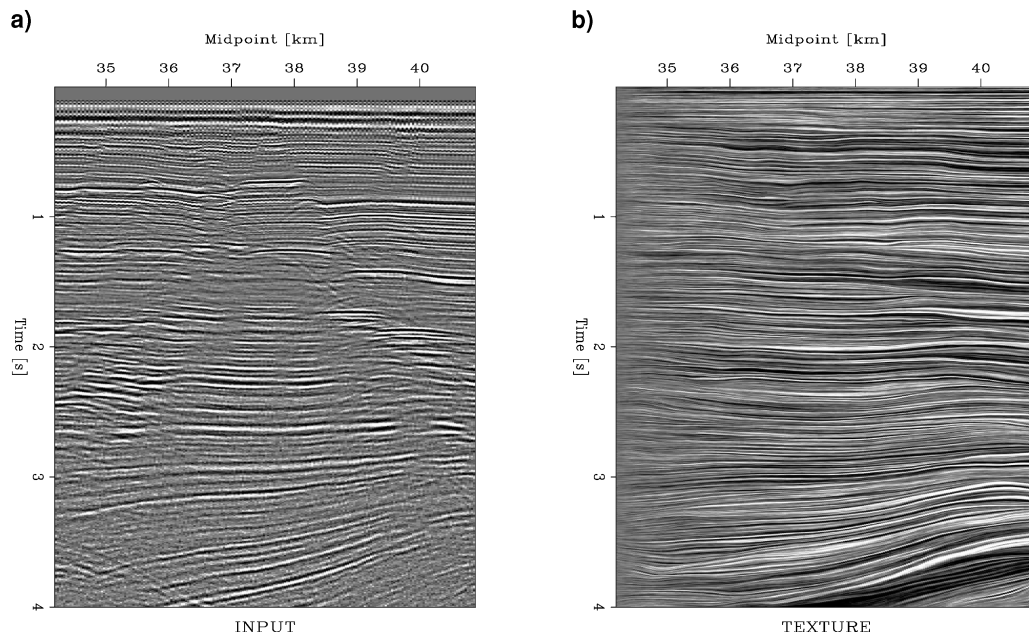


FIG. 9. Time section from the Gulf of Mexico. (a) Input data. (b) Its texture. The texture plot shows dominant local dips estimated from the data.

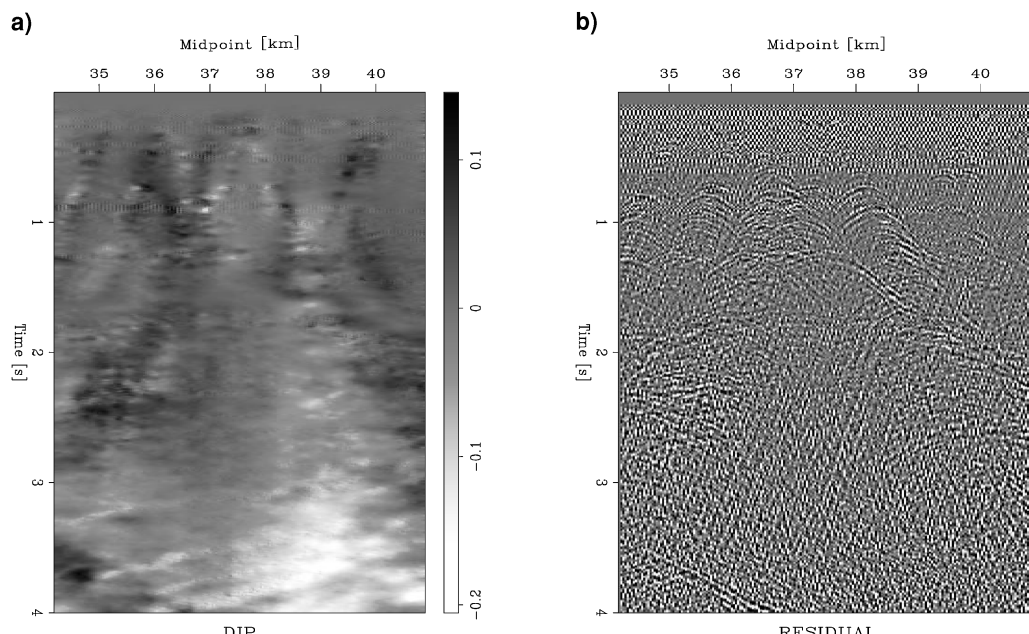


FIG. 10. Time section from the Gulf of Mexico. (a) Estimated dip field. (b) Prediction residual. The residual highlights diffraction events hidden under dominant reflections in the original data.

### Signal and noise separation

Signal and noise separation and noise attenuation are yet another important application of plane-wave prediction filters. Random noise attention has been successfully addressed by Canales (1984), Gulunay (1986), Abma and Claerbout (1995), and Soubaras (1995). A more challenging problem of coherent noise attenuation has only recently joined the circle of the prediction technique applications (Spitz, 1999; Brown and Clapp, 2000; Guitton et al., 2001).

The problem has a very clear interpretation in terms of the local dip components. If two components,  $s_1$  and  $s_2$ , are estimated

from the data, and if we can interpret the first component as signal and the second component as noise, then the signal and noise separation problem reduces to solving the least-squares system

$$\mathbf{C}(s_1)\mathbf{d}_1 \approx 0, \quad (19)$$

$$\varepsilon\mathbf{C}(s_2)\mathbf{d}_2 \approx 0 \quad (20)$$

for the unknown signal and noise components  $\mathbf{d}_1$  and  $\mathbf{d}_2$  of the input data  $\mathbf{d}$ :

$$\mathbf{d}_1 + \mathbf{d}_2 = \mathbf{d}. \quad (21)$$

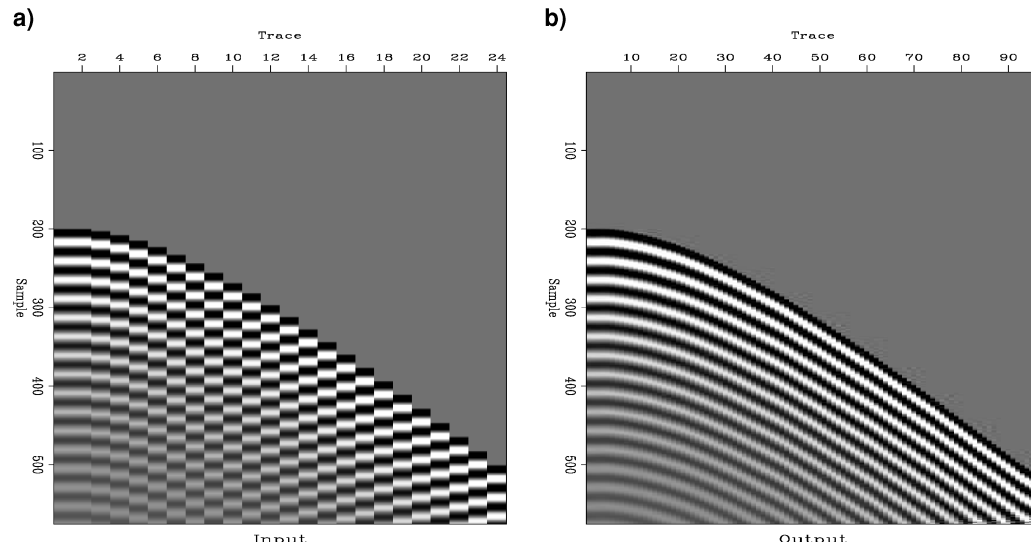


FIG. 11. Synthetic example of interpolation beyond aliasing with plane-wave destruction filters. (a) Input aliased data. (b) Interpolation output. Three additional traces were inserted between each of the neighboring input traces.

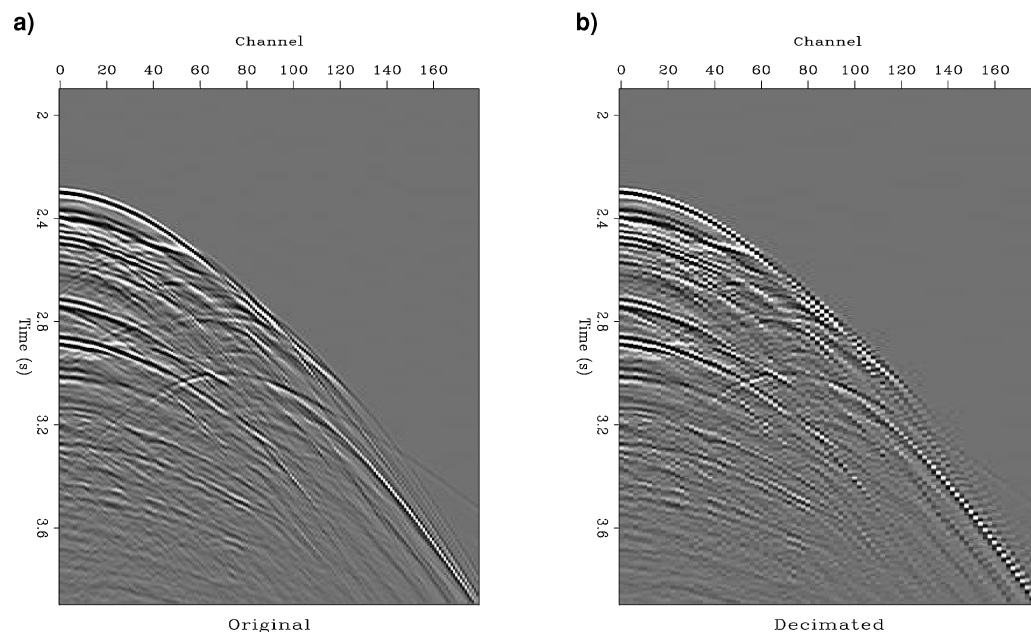


FIG. 12. A 2-D marine shot gather. (a) Original. (b) Subsampled by a factor of two in the offset direction.

The scalar parameter  $\varepsilon$  in equation (20) reflects the S/N ratio. We can combine equations (19)–(20) in the explicit system for the noise component  $\mathbf{d}_2$ :

$$\mathbf{C}(\mathbf{s}_1)\mathbf{d}_2 \approx \mathbf{C}(\mathbf{s}_1)\mathbf{d}, \quad (22)$$

$$\varepsilon\mathbf{C}(\mathbf{s}_2)\mathbf{d}_2 \approx 0. \quad (23)$$

Figure 16 shows a simple example of this approach. I estimated two dip components from the input synthetic data and separated the corresponding events by solving the least-

squares system [equations (22)–(23)]. The separation result is visually perfect.

Figure 17 presents a significantly more complicated case: a receiver line from of a 3-D land shot gather from Saudi Arabia contaminated with 3-D ground roll, which appears hyperbolic in the cross-section. The same data set has been used by Brown and Clapp (2000). The ground-roll noise and the reflection events have a significantly different frequency content, which might suggest separating them on the basis of frequency alone. However, the result of frequency-based separation, shown in

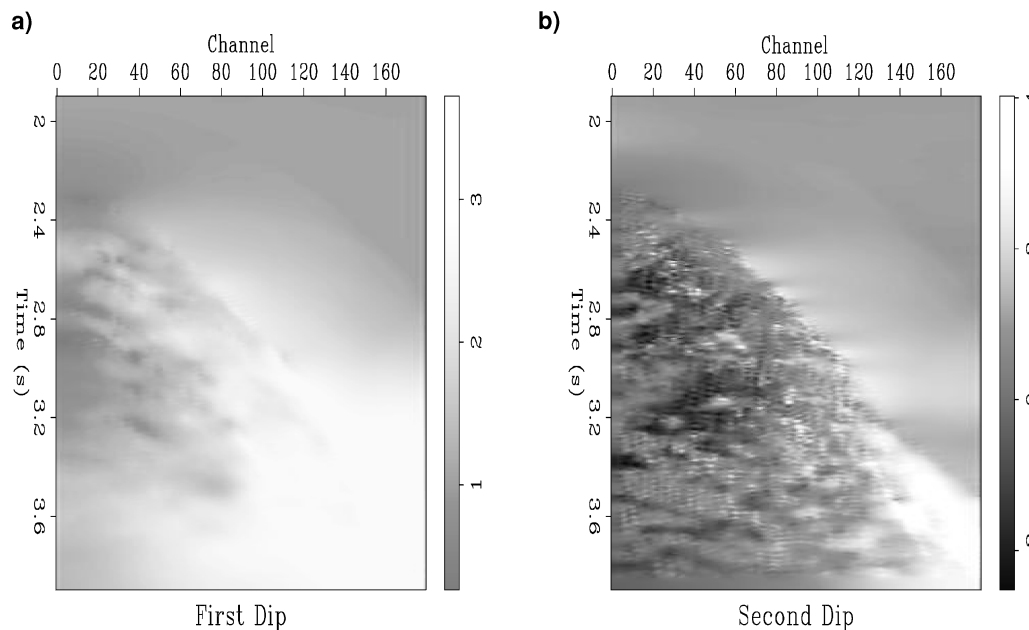


FIG. 13. Two components of the estimated dip field for the decimated 2-D marine shot gather.

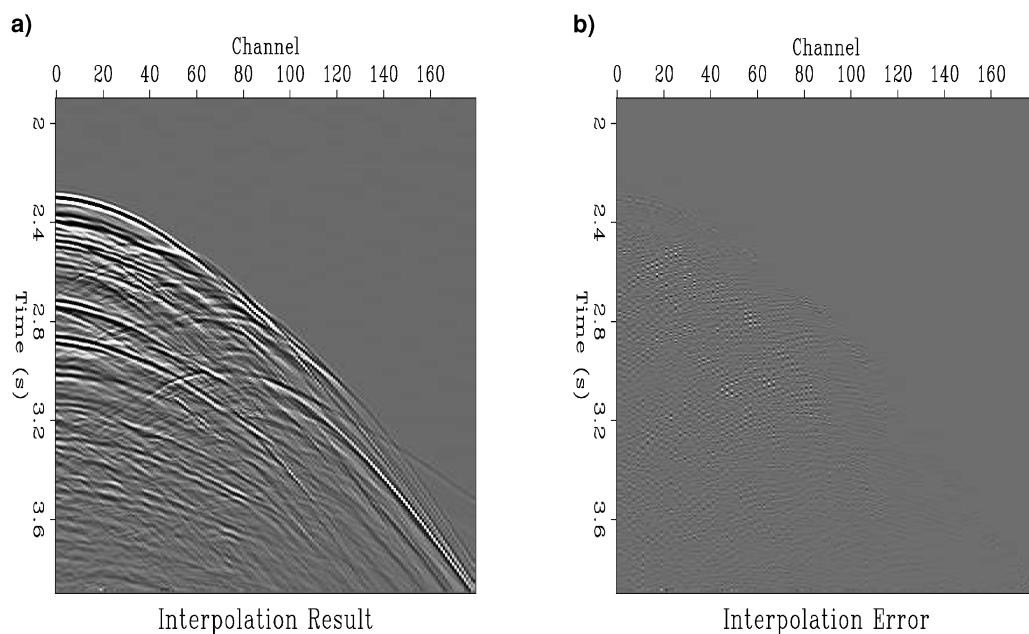


FIG. 14. (a) 2-D marine shot gather after trace interpolation. (b) Difference between the interpolated and the original gathers. The error is zero at the location of original traces and fairly random at the location of inserted traces.

Figure 18 is not ideal: part of the noise remains in the estimated signal after the separation. Changing  $\varepsilon$  in equation (23) could clean the signal estimate, but it would also bring some of the signal into the subtracted noise. A better strategy would be to separate the events by using both the difference in frequency and the difference in slope. For that purpose, I adopted the following algorithm.

- 1) Use a frequency-based separation (or, alternatively, a simple low-pass filtering) to obtain an initial estimate of the ground-roll noise.
- 2) Select a window around the initial noise. The further separation will happen only in that window.
- 3) Estimate the noise dip from the initial noise estimate.
- 4) Estimate the signal dip in the selected data window as the complementary dip component to the already known noise dip.
- 5) Use the signal and noise dips together with the signal and noise frequencies to perform the final separation. This is achieved by cascading single-dip plane-wave destruction filters with local 1-D, three-coefficient PEFs aimed at destroying a particular frequency.

The separation result is shown in Figure 19. The separation goal has been fully achieved: the estimated ground-roll noise is free of the signal components, and the estimated signal is free of the noise.

The left plot in Figure 20 shows another test example: a shot gather from Yilmaz and Cumro (1983), which is contaminated by nearly linear low-velocity noise. In this case, a simple dip-based separation was sufficient for achieving a good result. The algorithm proceeds as follows:

- 1) Bandpass the original data with an appropriate low-pass filter to obtain an initial noise estimate (Figure 20b).

- 2) Estimate the local noise dip from the initial noise model.
- 3) Estimate the signal dip from the input data as the complementary dip component to the already known noise dip.
- 4) Estimate the noise by an iterative optimization of system (22)–(23) and subtract it from the data to get the signal estimate.

Figure 21 shows the separation result. The signal and noise components are separated accurately.

These examples show that when the signal and noise components have distinctly different local slopes, we can successfully separate them with plane-wave destruction filters.

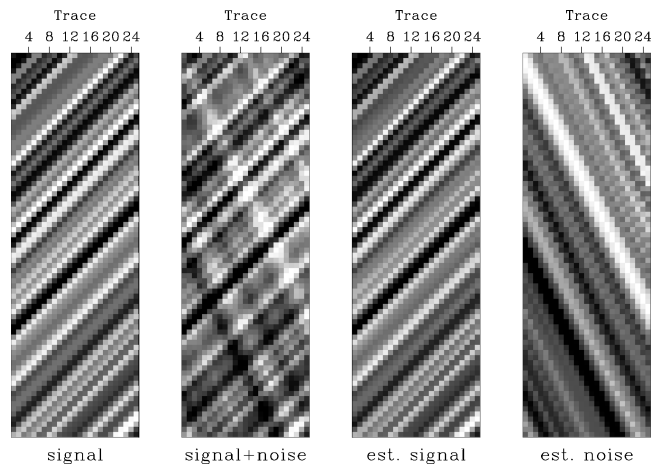


FIG. 16. Simple example of dip-based signal and noise separation. From left to right: ideal signal, input data, estimated signal, estimated noise.

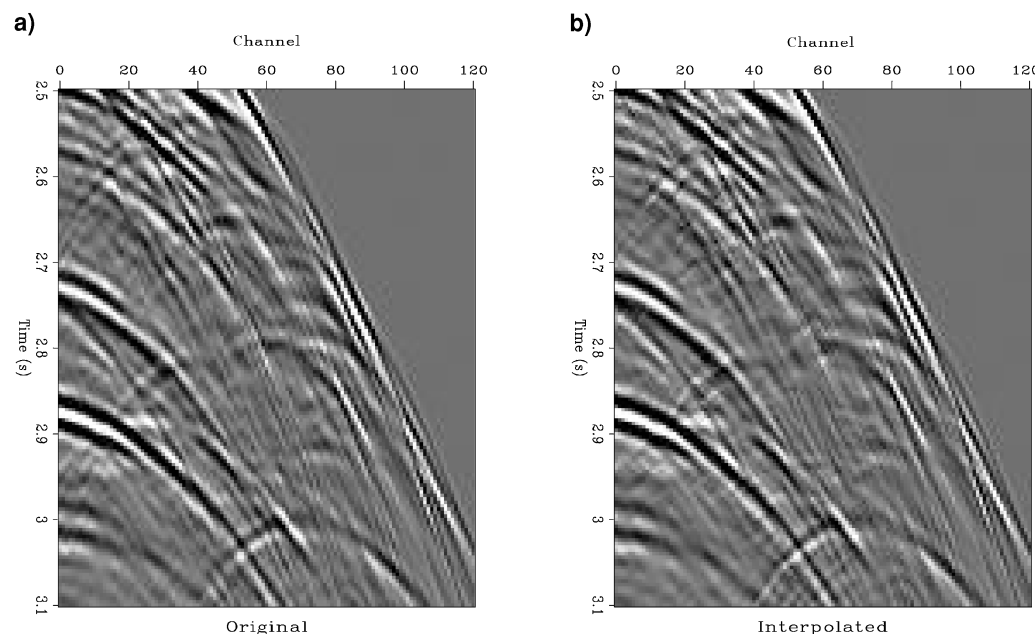


FIG. 15. Close-up comparison of (a) the interpolated and (b) the original data.

## CONCLUSIONS

Plane-wave destruction filters with an improved finite-difference design can be a valuable tool in processing multi-dimensional seismic data. They perform well in problems such as fault detection, missing data interpolation, and noise attenuation. Although only 2-D examples were demonstrated, it is straightforward to extend the method to 3-D applications by considering two orthogonal plane-wave slopes.

Plane-wave destructors and  $T$ - $X$  prediction-error filters are similar because (1) both types of filters operate in the original time-space domain of recorded data, (2) both filters aim to predict local plane-wave events in the data, and (3) in most problems, one filter type can be replaced by the other; certain

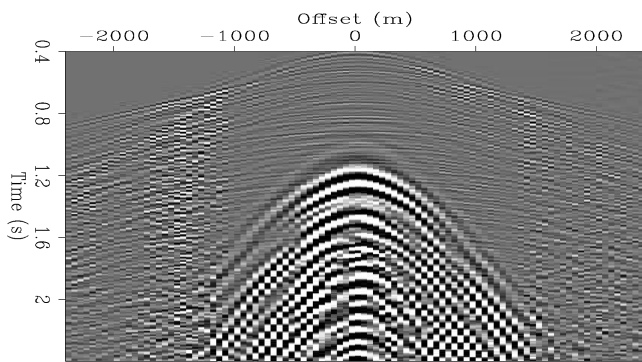


FIG. 17. Ground-roll-contaminated data from Saudi Arabian sand dunes. A receiver cable out of a 3-D shot gather.

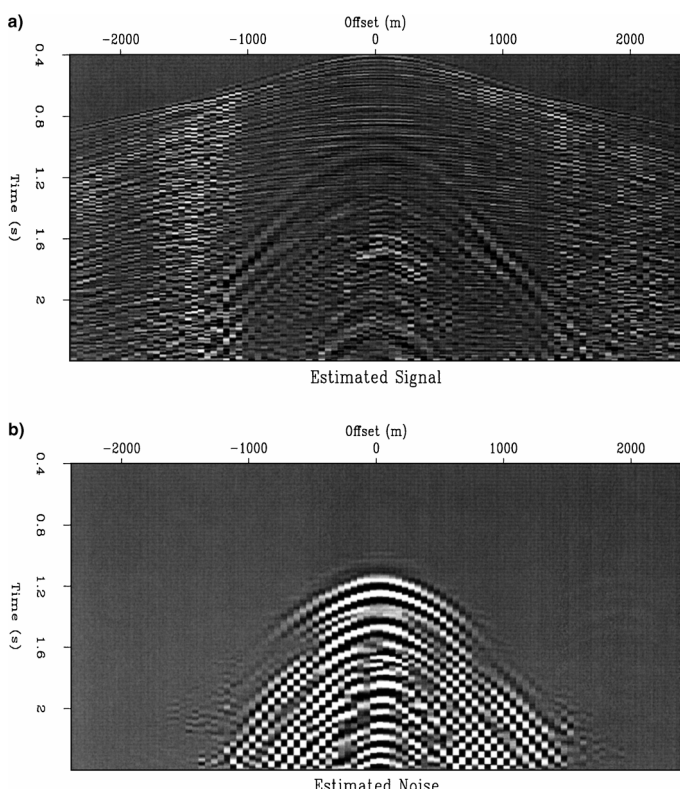


FIG. 18. Signal and noise separation based on frequency. (a) Estimated signal. (b) Estimated noise.

techniques, such as Claerbout's trace interpolation method, are common for both approaches.

There are three main differences between the two. First the design of plane-wave destructors is purely deterministic and follows the plane-wave differential equation. The design of a  $T$ - $X$  PEF has statistical roots in the framework of the maximum-entropy spectral analysis (Burg, 1975). In principle,  $T$ - $X$  PEFs can characterize more complex signals than local plane waves.

Second, in the case of PEFs, we estimate filter coefficients. In the case of plane-wave destructors, the estimated quantity is the local plane-wave slope. Several important distinctions follow from that difference:

- 1) The filter estimation problem is linear. The slope estimation problem, in the case of the improved filter design, is nonlinear but allows for an iterative linearization. In general, nonlinearity is undesirable because of local minima and the dependence on initial conditions. However, we can sometimes use it creatively. For example, it helped to avoid aliased dips in the trace interpolation example.
- 2) Nonstationarity is handled gracefully in the local slope estimation. No local windows are required to produce a smoothly varying estimate of the local slope. This is a much more difficult issue for PEFs because of the largely underdetermined problem.
- 3) Local slope has a clearly interpretable physical meaning, which allows for easy quality control of the results.

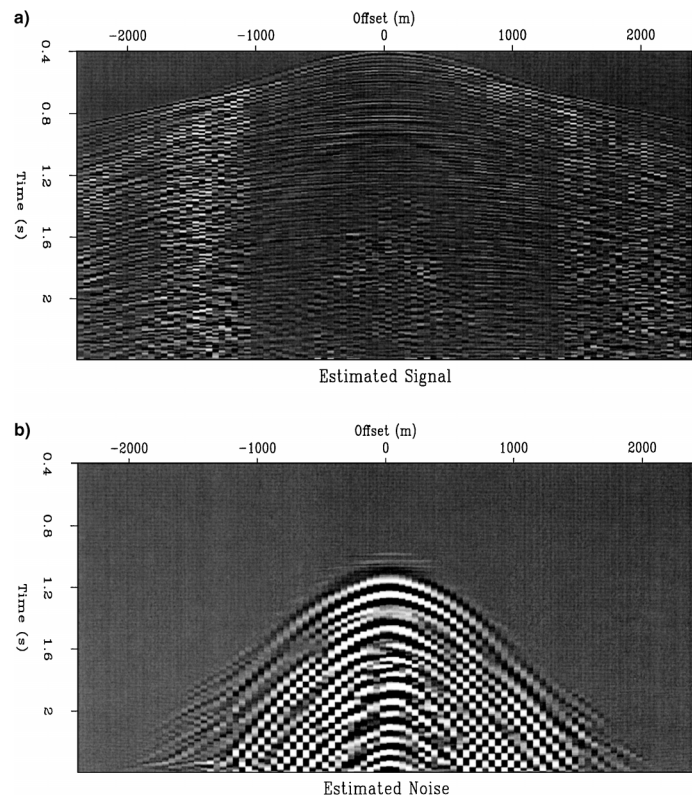


FIG. 19. Signal and noise separation based on both apparent dip and frequency in the considered receiver cable. (a) Estimated signal. (b) Estimated noise.

The coefficients of  $T$ - $X$  PEFs are much more difficult to interpret.

Finally, the efficiency of the two approaches is difficult to compare. Plane-wave destructors are generally more efficient to apply because of the small number of filter coefficients. However, they may require more computation at the estimation stage because of the nonlinearity problem.

#### ACKNOWLEDGMENTS

This work was partially accomplished at the Stanford Exploration Project (SEP). I thank Jon Claerbout, Robert Clapp, Matthias Schwab, and other SEP members for developing and maintaining the reproducible research technology, which helped this research. Suggestions from two anonymous reviewers helped to improve the paper.

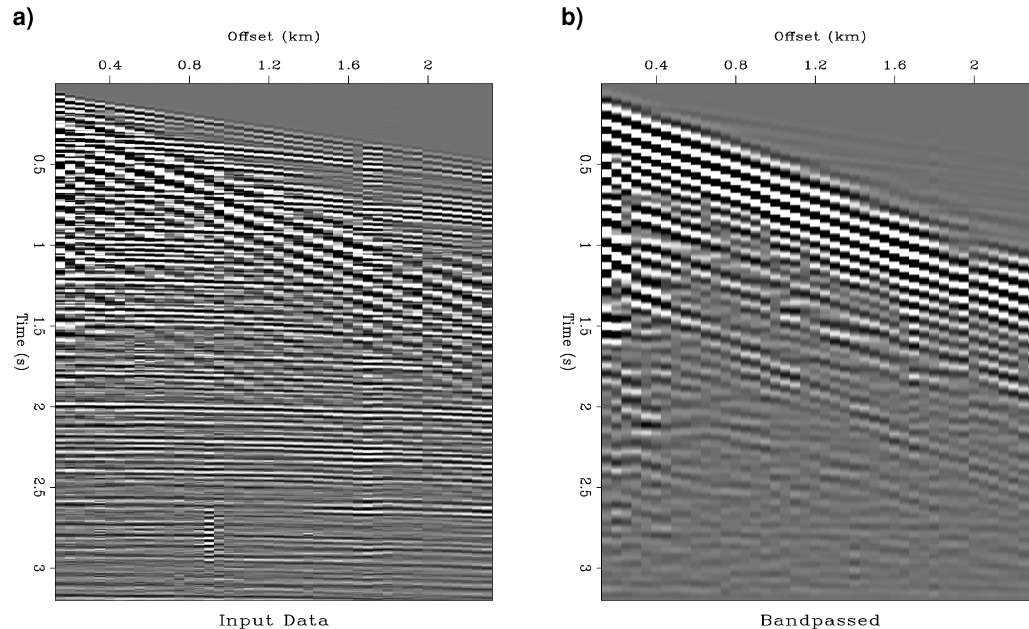


FIG. 20. (a) Input noise-contaminated shot gather. (b) Result of low-pass filtering. The filtered data is used as a noise model to estimate the noise dip.

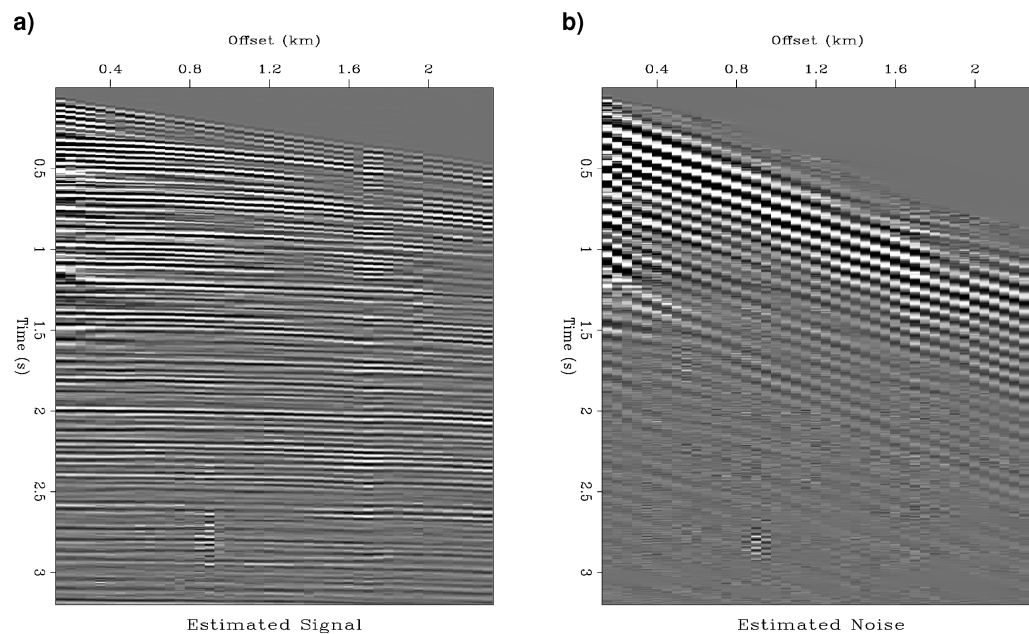


FIG. 21. Signal and noise separation based on dip. (a) Estimated signal. (b) Estimated noise.

## REFERENCES

- Abma, R., and Claerbout, J., 1995, Lateral prediction for noise attenuation by t-x and F-X techniques: *Geophysics*, **60**, 1887–1896.
- Bednar, J. B., 1998, Least squares dip and coherency attributes: 68th Ann. Internat. Mtg., Soc. Expl. Geophys., Expanded Abstracts, 653–655.
- Brown, M., and Clapp, R., 2000, T-X domain, pattern-based ground-roll removal: 70th Ann. Internat. Mtg., Soc. Expl. Geophys., Expanded Abstracts, 2103–2106.
- Burg, J. P., 1975, Maximum entropy spectral analysis: Ph.D. diss., Stanford Univ.
- Canales, L. L., 1984, Random noise reduction: 54th Ann. Internat. Mtg., Soc. Expl. Geophys., Expanded Abstracts, Session S10.1.
- Claerbout, J. F., 1992, Earth soundings analysis: Processing versus inversion: Blackwell Scientific Publications, Inc.
- , 1994, Applications of two- and three-dimensional filtering: 64th Ann. Internat. Mtg., Soc. Expl. Geophys., Expanded Abstracts, 1572–1575.
- , 1998, Multidimensional recursive filters via a helix: *Geophysics*, **63**, 1532–1541.
- , 1999, Geophysical estimation by example: Environmental soundings image enhancement: Stanford Exploration Project, <http://sepwww.stanford.edu/sep/prof/>.
- Claerbout, J., and Brown, M., 1999, Two-dimensional textures and prediction-error filters: 61st Mtg., Eur. Assoc. Expl. Geophys., Extended Abstracts, Session 1009.
- Clapp, R. G., 2001, Geologically constrained migration velocity analysis: Ph.D. diss., Stanford Univ.
- Clapp, R., Biondi, B., Fomel, S., and Claerbout, J., 1998, Regularizing velocity estimation using geologic dip information: 68th Ann. Internat. Mtg., Soc. Expl. Geophys., Expanded Abstracts, 1851–1854.
- Crawley, S., 2000, Seismic trace interpolation with nonstationary prediction-error filters: Ph.D. thesis, Stanford Univ.
- Crawley, S., Clapp, R., and Claerbout, J., 1999, Interpolation with smoothly nonstationary prediction-error filters: 69th Ann. Internat. Mtg., Soc. Expl. Geophys., Expanded Abstracts, 1154–1157.
- Fomel, S., 2001, Three-dimensional seismic data regularization: Ph.D. diss., Stanford University.
- Fomel, S., and Claerbout, J. F., 2003, Multidimensional recursive filter preconditioning in geophysical estimation problems: *Geophysics*, in press.
- Freeman, W. T., and Adelson, E. H., 1991, The design and use of steerable filters: *IEEE Trans. on Pattern Anal. and Mach. Intell.*, **1**, No. 9, 891–906.
- Guitton, A., Brown, M., Rickett, J., and Clapp, R., 2001, Multiple attenuation using a t-x pattern-based subtraction method: 71st Ann. Internat. Mtg., Soc. Expl. Geophys., Expanded Abstracts, 1305–1308.
- Gulunay, N., 1986, Fx decon and complex Wiener prediction filter: 56th Ann. Internat. Mtg., Soc. Expl. Geophys., Expanded Abstracts, Session POS2.10.
- Harlan, W. S., Claerbout, J. F., and Rocca, F., 1984, Signal/noise separation and velocity estimation: *Geophysics*, **49**, 1869–1880.
- Kim, S., and Symes, W. W., 1998, Smooth detectors of linear phase: *Inverse Prob.*, **14**, 101–112.
- Neidell, N. S., and Tamer, M. T., 1971, Semblance and other coherency measures for multichannel data: *Geophysics*, **36**, 482–497.
- Nichols, D., 1990, Estimation of missing data by least squares: Stanford Exploration Project Report **65**, 271–294.
- Schwab, M., 1998, Enhancement of discontinuities in seismic 3-D images using a Java estimation library: Ph.D. diss., Stanford Univ.
- Schwab, M., Claerbout, J., and Holden, C., 1996, Revealing geological discontinuities by plane reflector suppression: 66th Ann. Internat. Mtg., Soc. Expl. Geophys., Expanded Abstracts, 302–305.
- Simoncelli, E. P., and Farid, H., 1996, Steerable wedge filters for local orientation analysis: *IEEE Trans. on Image Proc.*, **5**, No. 9, 1377–1382.
- Soubaras, R., 1995, Prestack random and impulsive noise attenuation by F-X projection filtering: 65th Ann. Internat. Mtg., Soc. Expl. Geophys., Expanded Abstracts, 711–714.
- Spitz, S., 1991, Seismic trace interpolation in the *f*-*x* domain: *Geophysics*, **56**, 785–794.
- , 1999, Pattern recognition, spatial predictability, and subtraction of multiple events: *The Leading Edge*, **18**, No. 1, 55–58.
- Symes, W. W., 1994, The plane wave detection problem: *Inverse Probl.*, **10**, 1361–1391.
- Symes, W. W., and Carazzone, J. J., 1991, Velocity inversion by differential semblance optimization: *Geophysics*, **56**, 654–663.
- Yilmaz, O., and Cumro, D., 1983, Worldwide assortment of field seismic records: Western Geophysical Co.

## APPENDIX

## DETERMINING FILTER COEFFICIENTS BY TAYLOR EXPANSION

This appendix details the derivation of equations (9) and (10). The main idea is to match the frequency responses of the approximate plane-wave filters to the response of the exact phase-shift operator at low frequencies.

The Taylor series expansion of the phase-shift operator  $e^{i\omega\sigma}$  around the zero frequency  $\omega=0$  takes the form

$$e^{i\omega\sigma} \approx 1 + i\sigma\omega - \frac{\sigma^2\omega^2}{2} - i\frac{\sigma^3\omega^3}{6} + O(\omega^4). \quad (\text{A-1})$$

The Taylor expansion of the six-point implicit finite-difference operator takes the form

$$\begin{aligned} & \frac{B_3(Z_t)}{B_3(1/Z_t)} \\ &= \frac{b_{-1}Z_t^{-1} + b_0 + b_1Z_t}{b_1Z_t + b_0 + b_{-1}Z_t^{-1}} = \frac{b_{-1}e^{-i\omega} + b_0 + b_1e^{i\omega}}{b_1e^{-i\omega} + b_0 + b_{-1}e^{i\omega}} \\ &\approx 1 - \frac{2i(b_{-1} - b_1)\omega}{b_0 + b_{-1} + b_1} - \frac{2(b_{-1} - b_1)^2\omega^2}{(b_0 + b_{-1} + b_1)^2} \\ &+ \frac{i(b_{-1} - b_1)[b_0^2 - b_0(b_{-1} + b_1)4(b_{-1}^2 - 4b_{-1}b_1 + b_1^2)]\omega^3}{3(b_0 + b_{-1} + b_1)^3} \\ &+ O(\omega^4). \end{aligned} \quad (\text{A-2})$$

Matching the corresponding terms of expansions (A-1) and (A-2), we arrive at the system of nonlinear equations

$$\sigma = \frac{2(b_1 - b_{-1})}{b_0 + b_{-1} + b_1}, \quad (\text{A-3})$$

$$\sigma^2 = \frac{4(b_1 - b_{-1})^2}{(b_0 + b_{-1} + b_1)^2}, \quad (\text{A-4})$$

$$\begin{aligned} \sigma^3 \\ &= \frac{2(b_1 - b_{-1})[b_0^2 - b_0(b_{-1} + b_1) + 4(b_{-1}^2 - 4b_{-1}b_1 + b_1^2)]}{(b_0 + b_{-1} + b_1)^3}. \end{aligned} \quad (\text{A-5})$$

System (A-3)–(A-5) does not uniquely constrain the filter coefficients  $b_{-1}$ ,  $b_0$ , and  $b_1$  because equation (A-4) simply follows from (A-3) and because all of the coefficients can be multiplied simultaneously by an arbitrary constant without affecting the ratios in equation (A-2). I chose an additional constraint in the form

$$B_3(1) = b_{-1} + b_0 + b_1 = 1, \quad (\text{A-6})$$

which ensures that the filter  $B_3(Z_t)$  does not alter the zero frequency component. System (A-3)–(A-5) with the additional constraint (A-6) resolves uniquely to the coefficients of filter (9) in the main text:

$$b_{-1} = \frac{(1 - \sigma)(2 - \sigma)}{12}, \quad (\text{A-7})$$

$$b_0 = \frac{(2 + \sigma)(2 - \sigma)}{6}, \quad (\text{A-8})$$

$$b_1 = \frac{(1 + \sigma)(2 + \sigma)}{12}. \quad (\text{A-9})$$

The  $B_5$  filter of equation (10) is constructed in a completely analogous way, using longer Taylor expansions to constrain the additional coefficients. Generalization to longer filters is straightforward.

The technique of this appendix aims at matching the filter responses at low frequencies. One might construct different filter families by using other criteria for filter design (least-squares fit, equiripple, etc.).